

Large-eddy simulation of submerged marine vehicles

N. Morse, T. Kroll and K. Mahesh

(Department of Aerospace Engineering & Mechanics, University of Minnesota,
USA)

ABSTRACT

Large-eddy simulation (LES) using an unstructured overset grid method (Horne and Mahesh, 2019a,b) is used to explore several building-block problems of interest for submerged marine vehicles, including the bare and appended DARPA SUBOFF and the open and ducted propeller David Taylor Model Basin (DTMB) 4381 in crashback. An emphasis is placed on replicating the details of the experimental configurations and boundary conditions of these geometries, which is shown to be essential to reproduce certain aspects of their respective flow fields. The use of the overset grid method greatly reduces the set-up cost for these simulations, and LES results show good agreement with available experimental data. The consequences of boundary layer tripping methods and experimental confinement in crashback are discussed and physical insights made available from the LES data are presented.

INTRODUCTION

The performance of submerged marine vehicles is of critical importance for a variety of naval applications, although it is difficult to study numerically or experimentally due to the characteristically high Reynolds numbers and complex geometries of marine vehicles. These geometries are typically characterized by a long, slender axisymmetric hull with attached appendages and a rear-mounted propeller. For the large Reynolds numbers typical of such geometries, the hull boundary layer is turbulent. This leads it to become thick compared to the hull radius, especially at the tapering stern. The stern geometry also imposes streamline curvature and strong adverse pressure gradients, which may cause the hull boundary layer to separate. The thick hull boundary layer is ingested by the propeller, along with the wakes and junction vortices generated by the sail and four stern appendages. During decelerating maneuvers, the propeller is rotated in reverse while the vehicle is still moving in the forward direction. This off-design operating condition is called crashback, and

is characterized by an unsteady vortex ring created by the propeller-induced reverse flow. The reverse flow causes loss of stern appendage control authority, the propeller vortex ring is highly unsteady, and the propeller blades experience massive flow separation, creating low-frequency, high amplitude loads. Especially important are the loads projected onto the direction perpendicular to the propeller axis, which are termed side-forces. Since the propeller side-forces are typically located at a large distance from the vehicle center of mass, they induce significant moments.

Typically, down-scaled model experiments performed in a controlled environment are used to investigate different conditions of interest. Fabrication of suitable scale models that represent the complex geometries can present challenges. Another challenge is matching flow parameters such as the high Reynolds numbers in these controlled environments, typically water tunnels. To reproduce boundary layer transition that occurs at full-scale, trip wires are used at a fixed location. If experiments are performed in water or wind tunnels, the existence of tunnel boundaries can have consequences that deserve careful consideration. Some important factors are confinement effects that can lead to solid blockage and wake blockage effects (Barlow et al., 1999). Though theoretical blockage correction methods exist (Glauert, 1935), it is important to design water tunnels that minimize confinement, since it can impact the flow field around the model marine vehicle, differentiating it from the unconfined case.

While direct numerical simulation (DNS) of such high Reynolds number flows remains computationally infeasible due to resolution requirements (Moin and Mahesh, 1998), Reynolds-averaged Navier-Stokes (RANS) and large-eddy simulation (LES) have shown promise for these flows. Yang and Löhner (2003) and Kim et al. (2013) demonstrated the ability of RANS to capture mean quantities around hull geometries, but RANS has been shown to fail for more complex flow configurations, including crashback (Davoudzadeh et al., 1997; Chen and Stern, 1999). LES has been shown to be

a good middle ground between RANS and DNS, as the method directly resolves large, energy-containing scales and models the effect of smaller scales. LES has shown good performance for a variety of marine flows, including crashback (Chang et al., 2008; Verma et al., 2012; Jang and Mahesh, 2013; Kumar and Mahesh, 2017, 2018; Kroll and Mahesh, 2022), and was used to study maneuvering building-block problems in Kroll et al. (2020).

Aside from the limitations of high Reynolds numbers, a significant challenge of maneuvering calculations is the requirement for the numerical method to resolve the relative movements of bodies within the simulation. Horne and Mahesh (2019a,b) developed an unstructured overset method for LES and DNS of high Reynolds number flows based on the finite volume method of Mahesh et al. (2004), and we use this overset LES method for the present work. The overset method decomposes the computational domain into different arbitrarily overlapping and moving meshes using an Arbitrary Lagrangian-Eulerian (ALE) formulation. This method therefore allows for moving body-fitted meshes to maintain the required near-wall spacing for moving bodies at high Reynolds numbers.

In this work we consider the body of a marine vehicle by studying both the bare (un appended) DARPA SUBOFF as well as the appended hull, which has an added fairwater (sail) and four stern appendages arranged in a cross shape, as shown in figure 1. Huang et al. (1992) conducted experiments of flow over both the bare and appended hull geometries at a length-based Reynolds number of $Re_L = 1.2 \times 10^7$, while Jiménez et al. (2010a) studied the wake of the bare hull over a Reynolds number range of 1.1×10^6 to 6.7×10^7 . The Reynolds number $Re_L = U_\infty L / v$ is defined using a length scale, L , the free-stream velocity, U_∞ , and the kinematic viscosity, v . Jiménez et al. (2010b) also studied the appended hull configuration over a Reynolds number range of 4.9×10^5 to 1.8×10^6 . Kumar and Mahesh (2018) and Morse and Mahesh (2021) studied flow over the axisymmetric bare hull at $Re_L = 1.1 \times 10^6$, demonstrating good agreement with experiments and studying the wake evolution and streamline curvature, respectively. Posa and Balaras (2016) performed wall-resolved LES over the appended hull configuration at $Re_L = 1.2 \times 10^6$, which was followed by a partially wall-modeled LES at $Re_L = 1.2 \times 10^7$ (Posa and Balaras, 2020), with both computations showing good agreement with experiments. Kroll et al. (2020) demonstrated the capability of overset LES to simulate the appended hull at $Re_L = 1.2 \times 10^6$ through comparison of surface quantities to the data of Huang et al. (1992). Chase and Carrica (2013) also used an overset method with delayed detached eddy simulation (DDES) to simulate the appended SUBOFF and E1619 propeller in self-propelled and maneuvering conditions.

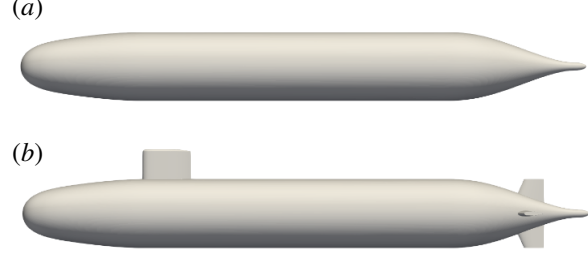


Figure 1: Depiction of the axisymmetric bare hull DARPA SUBOFF (a) and the appended DARPA SUBOFF (b).

In regards to propulsion of a marine vehicle, we consider the case of a ducted propeller in crashback. Propeller DTMB 4381 has been studied experimentally in forward mode and crashback for open propellers (Jiang et al., 1997; Jessup et al., 2004, 2006). It has also been studied computationally using LES (Vyšohlid and Mahesh, 2006; Chang et al., 2008; Verma et al., 2012; Jang and Mahesh, 2013; Kumar and Mahesh, 2017; Kroll and Mahesh, 2022). Kroll et al. (2020) validated the present overset LES method for propeller P4381 in the open configuration for both forward mode and crashback, comparing well to previous experiments and computations.

A ducted propeller in crashback presents additional challenges to maneuverability of a marine vehicle. Jessup et al. (2006); Swithenbank et al. (2008); Donnelly et al. (2010) studied propeller P4381 experimentally with a duct and noted that the side-forces for this case are up to three times the magnitude measured in the open configuration. This case presents additional challenges to study computationally, with the need to represent the complex geometry of the propeller, duct and stator blades as well as the small tip-gap between the propeller blades and the duct surface. In addition, the experiments note that there are potential water tunnel confinement effects on the data. Previous computations using LES with a sliding interface method were used to study the ducted configuration (Jang and Mahesh, 2012), although the flow was not studied statistically. More recently, Kroll and Mahesh (2022) used the present overset methodology to study the same configuration, showing good agreement with experiments. They included the 36-inch Variable Pressure Water Tunnel (VPWT) in the computation and detailed the main mechanisms behind the high side-forces relevant to maneuvering. In this work, we show that including the VPWT is essential to the validation of LES simulations of crashback for both the open and ducted propeller. We also present some of the insights into the physical mechanisms that lead to high side-forces of the ducted propeller in

crashback.

With the aforementioned numerical challenges in mind, this work is a continuation of the computations in Kroll et al. (2020), where several building-block computations for maneuvering problems were presented, including flow over the bare and appended SUBOFF hull geometries as well extensive validation of the overset method for forward mode and crashback of the P4381 propeller. In the present work, we build upon the contributions and simulation capability demonstrated by Kroll et al. (2020) by:

1. discussing how the inclusion of experimental tripping affects the overall flow field around the bare and appended SUBOFF hulls,
2. presenting curved boundary layer analysis made possible by LES of the bare SUBOFF hull,
3. demonstrating that the inclusion of experimental water tunnel geometry and the resulting confinement effects are important for validation of the open and ducted propeller P4381 in crashback, and
4. providing insights from LES for the high side-forces produced for a ducted P4381 propeller in crashback.

These studies are made possible by leveraging the capabilities of the overset method developed by Horne and Mahesh (2019a,b), which allows for simpler body-fitted meshes around complex geometries with relevant local resolutions. This overset method was developed for direct numerical simulation and LES of complex geometries by emphasizing conservation of kinetic energy and using a penalty method to enforce pressure continuity at interpolation boundaries. For reliable numerical code validation, it is essential to match the model down-scaled experiments and their boundary conditions. The overset method makes it possible to represent not only the complex geometries being studied, but also the specific geometries used in the experiments, including the experimental trip wires and tunnel geometries.

SIMULATION DETAILS

Numerical Method

The simulation of complex maneuvering bodies at high Reynolds numbers presents several challenges. These include the ability of the numerical method to handle complex geometries and their relative movement as well as robustness for high Reynolds number calculations. The unstructured overset grid method of Horne and Mahesh (2019a,b) tackles these challenges

using an unstructured overset grid method based on the finite-volume method developed by Mahesh et al. (2004), which emphasizes discrete kinetic energy conservation to ensure robustness without added numerical dissipation. This lack of numerical dissipation prevents artificial damping of small scales at high Reynolds numbers while retaining numerical stability, which is especially critical for LES. This method has been successful in simulating a variety of complex marine flows (Verma et al., 2012; Kumar and Mahesh, 2017; Jang and Mahesh, 2013; Kumar and Mahesh, 2018).

In an overset method, redundant cells in overlapping meshes are removed, revealing exposed cell faces which require boundary conditions that are provided by the interpolation of the flow field from neighboring meshes. Horne and Mahesh (2019b) developed a novel supercell interpolation for velocity to ensure bounded kinetic energy of the interpolation boundary conditions along with a penalty method for pressure continuity. Horne and Mahesh (2019a) addressed the scaling challenges typical of overset methods by employing a novel communication strategy, allowing the method to scale to $O(10^5)$ meshes and processors.

The incompressible Navier-Stokes equations with an Arbitrary Lagrangian-Eulerian (ALE) formulation coupled to a six degree-of-freedom (6-DOF) solver are used, allowing for the simulation of bodies with prescribed or free motion. For LES, large scales are directly accounted for by the spatially filtered Navier-Stokes equations, and small scales are modeled. The filtered Navier-Stokes equations with the ALE formulation are

$$\begin{aligned} \frac{\partial \bar{u}_i}{\partial t} + \frac{\partial}{\partial x_j} (\bar{u}_i \bar{u}_j - \bar{u}_i V_j) &= - \frac{\partial \bar{p}}{\partial x_i} + \nu \frac{\partial^2 \bar{u}_i}{\partial x_j \partial x_j} - \frac{\partial \tau_{ij}}{\partial x_j}, \\ \frac{\partial \bar{u}_i}{\partial x_i} &= 0, \end{aligned} \quad (1)$$

where u_i is the velocity in the inertial frame, p is the pressure, the overbar ($\bar{\cdot}$) denotes the spatial filter and $\tau_{ij} = \bar{u}_i \bar{u}_j - \bar{u}_i \bar{u}_j$ is the sub-grid stress tensor. The mesh velocity V_j is included in the convection term to avoid tracking multiple frames of reference. To model the sub-grid stress terms, the dynamic Smagorinsky model proposed by Germano et al. (1991) and modified by Lilly (1992) is used, where a Lagrangian time scale is dynamically computed based on surrogate-correlation of the Germano-identity error (Park and Mahesh, 2009). The equations are advanced in time using Crank-Nicolson or second-order backward differencing implicit time integration with a predictor-corrector formulation. A multi-point flux approximation developed by Horne and Mahesh (2021) is used to construct accurate gradients on skewed meshes.

Geometry and Computational Mesh

Bare hull DARPA SUBOFF

Wall-resolved LES of the bare hull DARPA SUBOFF (figure 1a) is performed at a Reynolds number of $Re_L = 1.1 \times 10^6$ based on the free-stream velocity and hull length (L), matching the experiments of Jiménez et al. (2010a). Figure 2 shows the domain size for the hull computations. The inflow boundary is placed a distance of $3D_H$ from the front of the hull, while the outflow boundary is $17.2D_H$ from the tip of the stern, where D_H is the maximum hull diameter. The radial boundaries are located at $6D_H$ from the hull centerline to minimize confinement effects. For the bare hull case, the domain is split into three grids for the background, hull, and wake, as shown with black, red, and blue outlines respectively in figure 2. The free-stream boundary conditions are imposed at the upstream and radial boundaries of the background grid, while a convective outflow condition is imposed at the downstream boundary. This leaves the hull and wake refinement grids, which are refined to capture the fine near-wall boundary layer structures and the wake evolution. The hull grid has a nominal grid resolution of $\Delta y^+ = 1$, $\Delta x^+ = 33$, and $a^+\Delta\theta = 11$, where a is the local radius of transverse curvature at the mid hull. Additional details of the computational grid may be found in Morse and Mahesh (2021). The sizes of the background, hull, and wake grids are shown in table 1.

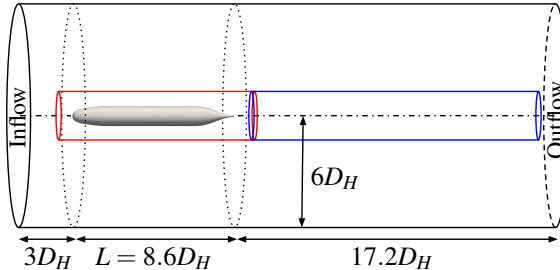


Figure 2: Computational domain for simulation of the bare hull SUBOFF configuration. The background grid is shown with a black outline, while the hull and wake refinement grids are shown as red and blue, respectively.

An important consequence of the $O(1$ million) hull Reynolds number is that the momentum-thickness Reynolds number, $Re_\theta = \theta U_\infty / v$, of the hull boundary layer (where θ is the boundary layer momentum thickness) is lower than 2000 over most of the hull. Schlatter and Örlü (2012) analyzed direct numerical simulation (DNS) of several flat-plate turbulent boundary layers at moderate Re_θ and found significant differences between simulations attributed to downstream dependence on the employed tripping method. They

conclude that if transition is initiated within the boundary layer at $Re_\theta < 300$, quantities agree well throughout the inner and outer layer after the boundary layer has reached $Re_\theta > 2000$, given that the boundary layer is not over- or under-tripped. These findings indicate that simulation results may be sensitive to tripping effects, given the moderate Re_θ of the hull boundary layer. Based on the resulting implications on Reynolds number scaling of down-scaled experiments and computations, in this work we analyze two methods of tripping the hull boundary layer.

The first tripping method involves imposing a wall-normal blowing velocity of $0.06U_\infty$ at $x/D_H = 0.75$ from the front of the hull, matching the experimental trip location of Jiménez et al. (2010a). The wall-normal blowing velocity was specified as the minimum magnitude required to promote quick transition of the boundary layer. This method has been shown to effectively trip the hull boundary layer, producing developed turbulent boundary layers by the mid hull (Kumar and Mahesh, 2018; Kroll et al., 2020; Morse and Mahesh, 2021). However, the detailed effects of this tripping method compared to the experimental trip wire have not been explored. Therefore, in this work we directly resolve the $0.005D_H$ diameter experimental trip wire of Jiménez et al. (2010a) by adding an additional overset grid (table 1) to resolve flow around the trip. The overset method makes it possible to reuse the background, hull, and wake grids for the resolved trip wire calculation, greatly reducing set-up time and permitting direct comparison of results. Although an extensive grid refinement study of the trip grid was not made due to the size of the computation ($O(10000)$ processors), care is taken to resolve the trip geometry as well as provide matching grid resolution at the interpolation boundaries to the hull grid. Computations with the blowing trip method are performed with a non-dimensional time step of $\Delta t U_\infty / D_H = 0.0012$, while the computations with the resolved trip wire are limited to half this time step due to the fine resolution near the trip wire. The non-dimensional time step for this case based on the trip wire height was $\Delta t U_\infty / h_{\text{trip}} = 0.12$ and the trip is verified to promote quick transition the boundary layer behind the trip wire.

Table 1: Details for the bare hull SUBOFF overset grids including number of control volumes and number of processors.

Grid	CVs	Procs
Background	113M	1540
Hull	429M	5676
Wake	170M	2288
Trip wire	17M	220

Appended DARPA SUBOFF

Wall-resolved LES of flow over the appended SUBOFF geometry (figure 1b) are performed at a length-based Reynolds number of $Re_L = 1.2 \times 10^6$ to match the experiments of Jiménez et al. (2010b). The overset method allows for computations of the appended hull to reuse the background, hull, and wake refinement grids from the bare hull computations (table 2), leaving the domain size and far-field boundary conditions unchanged from what was described in the previous section. Additional grids for the sail and four stern appendages are added, as shown in table 2.

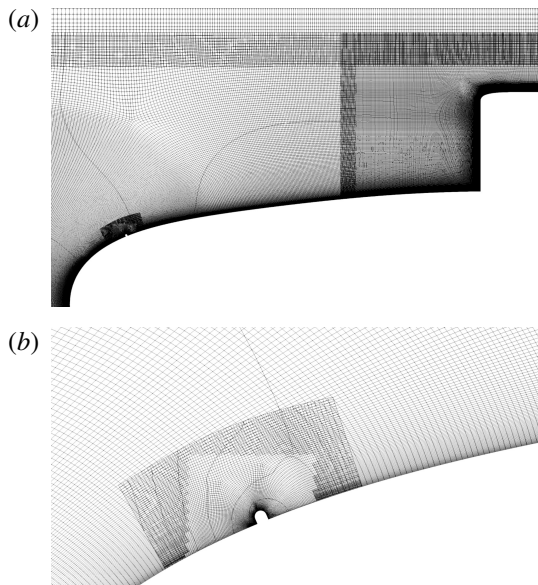


Figure 3: Symmetry plane views of the appended hull grids: (a) slice of the hull, sail, trip wire, and background grids, and (b) zoomed-in view of the trip wire grid.

As with the bare hull computations, we also compare the effects of a numerical trip using a blowing velocity of $0.06U_\infty$ to a resolved trip wire. Note that the appended hull experiments of Jiménez et al. (2010b) use a trip wire located at $x/D_H = 0.25$ from the front of the hull, compared to the trip at $x/D_H = 0.75$ that was used by Jiménez et al. (2010a) for the bare hull. We therefore use the trip geometry of Jiménez et al. (2010b) for the present computations. The trip wire is also comparatively larger for the appended hull, with a trip wire diameter of $0.0098D_H$, which is almost double that of the bare hull trip wire. The larger size of the trip wire may be motivated by the strong favorable pressure gradient at the $x/D_H = 0.25$ trip position, although the trip height now becomes much taller than the laminar boundary layer thickness at this position. Figure 3 shows a slice of the computational grids with the trip through

the sail symmetry plane. This is done to visualize the overlap between the hull, sail, trip wire, and background grids in figure 3a and highlighting the grid resolution around the trip wire in figure 3b. Computations without the resolved trip wire are performed at a non-dimensional time step of $\Delta t U_\infty / D_H = 0.0006$, while computations with the resolved trip wire are run at $\Delta t U_\infty / D_H = 0.00042$.

Finally, Liu and Huang (1998) reports the presence of trips at 5% chord of the sail and stern appendages in the experiments conducted by Huang et al. (1992), while Jiménez et al. (2010b) does not report any tripping for the appendages in their experiment. Kroll et al. (2020) reported satisfactory agreement of C_p on appendages from LES to the experimental C_p measurements of Huang et al. (1992), although some differences were noted for C_p on the sail. Therefore, in this study we investigate the effect of adding trips on the sail and stern appendages compared to the un-tripped case. The tripping is performed by wall-normal blowing at $0.06U_\infty$ to match the hull blowing velocity.

Table 2: Details for the appended SUBOFF overset grids including number of control volumes and number of processors.

Grid	CVs	Procs
Background	Reused (see table 1)	
Hull	Reused (see table 1)	
Wake	Reused (see table 1)	
Sail	91M	1188
Stern appendages	6M \times 4	176 \times 4
Trip wire	16M	220

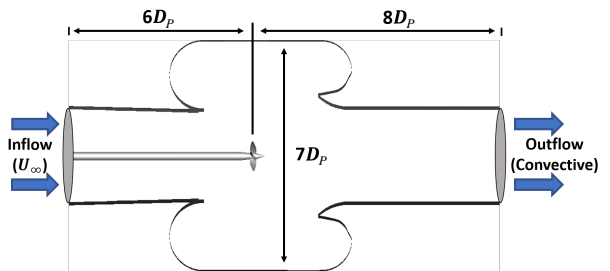


Figure 4: A cross-section of the computational domain which includes the open jet section of the VPWT geometry and propeller DTMB 4381. Boundary conditions are also shown. The VPWT wall and hub surface have a no slip boundary condition. D_P is the propeller disk diameter.

36-inch Variable Pressure Water Tunnel

Jessup et al. (2004, 2006); Swithenbank et al. (2008); Donnelly et al. (2010) performed down-scaled model experiments of DTMB 4381 in crashback for an open and ducted configuration. These experiments were performed inside the open jet section of the 36-inch VPWT. To gain some insights on the flow, LES of the VPWT geometry without a propeller is run at the Reynolds number $Re_D = 561,000$, based on the propeller disk diameter ($D_P = 12.0\text{in}$). Figure 4 shows the problem dimensions and boundary conditions. The origin is located where the experimental propeller is centered and the inflow boundary condition is located $6D_P$ upstream. The inflow is set so that the free-stream velocity U_∞ is achieved at $1.67D_P$ downstream of the tunnel nozzle outlet, similar to the experiments. $8D_P$ downstream of the propeller center, a convective boundary condition is set and no slip boundary conditions are set on the VPWT wall surfaces. The VPWT wall normal resolution has a height of $0.0017D_P$ and a growth ratio of 1.01. The non-dimensional time step is $\Delta t U_\infty / D_P = 1.667 \times 10^{-4}$. The simulation is ran for 9 full domain passes. The overset method is not utilized for this simulation as a single grid representing the VPWT is sufficient and will later be used as a background grid for the propeller cases. Additional details on the grid size and partitioning are in table 3. More detailed information on the VPWT geometry is provided in Jessup et al. (2004, 2006); Swithenbank et al. (2008); Donnelly et al. (2010).

Table 3: Details for the grids used for the LES of the VPWT geometry, including the number of control volumes and the number of processors.

Grid	CVs	Procs
VPWT	17.6M	352

Open and Ducted Crashback for Propeller P4381

Marine propeller DTMB 4381 is a five-bladed, right-handed propeller with variable pitch, and no skew or rake. More details about the propeller can be found in Jessup et al. (2004, 2006). Two cases are simulated in crashback at an advance ratio of $J = -0.82$ and at the Reynolds number $Re_D = 561,000$ based on the propeller diameter. J and Re_D are defined by

$$J = \frac{U_\infty}{nD_P}, \quad Re_D = \frac{U_\infty D_P}{\nu} \quad (2)$$

where U_∞ is the free-stream velocity, $D_P = 12.0\text{in}$ is the propeller disk diameter, n is the rotational speed, and ν is the kinematic viscosity.

The propeller loads are non-dimensionalized as follows. ρ is the fluid density, and the thrust T is defined

as the axial component of the force. The axial component of the propeller torque is Q . F_H and F_V are the horizontal and vertical components of the force, whose vector sum yields the total side-force F_T . The non-dimensional thrust K_T , torque coefficient K_Q and side-force coefficient K_S are defined as:

$$K_T = \frac{T}{\rho n^2 D_P^4}, \quad K_Q = \frac{Q}{\rho n^2 D_P^5}, \quad K_S = \frac{\sqrt{F_H^2 + F_V^2}}{\rho n^2 D_P^4} \quad (3)$$

Taking the time average of these quantities, $\langle K_T \rangle$ represents the mean of the coefficient K_T and $\sigma(K_T)$ the standard deviation.

Jessup et al. (2004, 2006) hypothesized that water tunnel effects, including confinement, could affect their results, especially the loads. Previous LES of open and ducted propellers in crashback (Vyšohlid and Mahesh, 2006; Chang et al., 2008; Jang and Mahesh, 2012, 2013; Kroll et al., 2020) did not include the VPWT geometry. For an open (non-ducted) propeller, there was a noticeable difference in the loads, more specifically K_T and K_Q . The magnitude of these loads in these publications were found to lie in between the VPWT and open water (OW) experiments of Ebert et al. (2007), which were performed in the Naval Surface Warfare Center, Carderock Division (NSWCCD). Jessup et al. (2006) mentioned that there is no detailed understanding of this load difference but attributed it to potential water tunnel confinement effects. These effects are expected to be worse for a ducted propeller which has a larger vortex ring, which may interact more with the tunnel outlet shear layer. To improve understanding of potential confinement effects and to better match the experimental boundary conditions, the VPWT geometry is included in the present simulations. The empty VPWT and open propeller with the VPWT geometry are simulated to show that it is essential to include the VPWT in order to validate the more complex ducted crashback case presented by Kroll and Mahesh (2022).

The first crashback case is the open configuration, the problem dimensions and boundary conditions are shown in figure 4. According to data from Jessup et al. (2006), at this J there was a more significant difference in the loads compared to lower magnitude J . Two grids are utilized for this computation. The background grid contains the VPWT and part of the hub, while the overset grid contains the propeller and a portion of hub as well. The overset grid is rotated at the rotational velocity $\omega = 2\pi n$ to match the advance ratio J . The hub surface has a no slip boundary condition, except for the overset grid portion. The blade mesh surfaces and the hub surface contained in the overset propeller mesh have a boundary condition of $v = \omega \times R$. For the background mesh, a cylindrical cut is used to remove

redundant control volumes in the location of the overset grid. The design ensures enough overlap between meshes so that viable interpolation partner pairs are found for the interpolation boundary control volumes. Similar to Jang and Mahesh (2013); Verma et al. (2012); Kroll et al. (2020), the propeller mesh uses a pill-box of tetrahedral cells around the blades. Meanwhile, on the blade surface, four prism layers are extruded from a first-layer height of $0.0017D_P$ at a growth ratio of 1.01. On other surfaces, the wall normal resolution is the same as on the blades. More information on the size and partitioning of the meshes is presented in table 4.

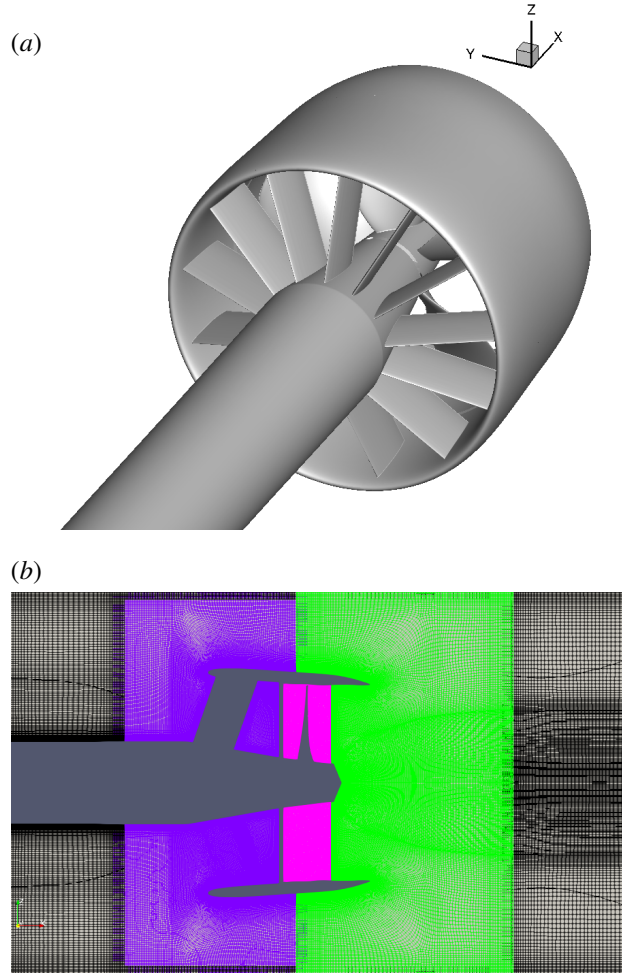


Figure 5: (a) The geometries of the propeller, duct and stator blades (Kroll and Mahesh, 2022). (b) A cross-section showing the mesh configuration and overlap of all 4 grids (Kroll and Mahesh, 2022). The background grid which also contains the VPWT walls overlaps the grids around the duct and propeller.

Table 4: Details for the grids used for the LES in crashback, including the number of control volumes and the number of processors.

Grid	CVs	Procs
Background (VPWT)	31.8M	544
Propeller	13.2M	384
Total	45.0M	928

The second case we consider are the results from the ducted configuration of Kroll and Mahesh (2022), compared to the experiments by Jessup et al. (2006); Swithenbank et al. (2008); Donnelly et al. (2010). The domain dimensions are the same as the first case, as depicted in figure 4. In the experiments, added around propeller DTMB 4381 is a neutrally loaded duct constructed using Stereolithography (SLA) plastic and designed to add no additional propulsor loading at the design advance ratio of $J = 0.889$. The duct has 13 aligned support vanes or stator blades (figure 5a). Four unstructured grids are used to represent the flow domain, as depicted in figure 5b. On the background grid is the VPWT geometry as well as the inlet and the outlet boundary conditions. A total of three overset grids are used to represent the duct and the propeller. For the duct, two grids are used: an upstream portion containing part of the duct with the stator blades (purple in figure 5b) and a downstream portion containing the rest of the duct (green in figure 5b). The surfaces contained on these grids have no-slip boundary conditions. The third grid contains the propeller, all of the 5 rotor blades, and part of the inner-duct, as shown in pink in figure 5b. This is the only grid with prescribed movement. It is rotated at the rotational velocity ω to match the advance ratio while $v = \omega \times R$ boundary conditions are prescribed on the rotor blades and hub surfaces contained in this grid. The boundary conditions on the inner-duct portion of the grid are set to no-slip. More information on the size and partitioning of the meshes is presented in table 5.

Table 5: Details of the four grids used for the ducted propeller case, including the number of control volumes and the number of processors used. The background grid is meant to contain all the other grids within it and contains the VPWT geometry. The propeller grid is the only dynamic one, to represent the propeller rotation.

Grid	CVs	Procs
Background (VPWT)	28.7M	960
Propeller	19.1M	732
Upstream Duct and Stator	16.6M	710
Downstream Duct	5.8M	238
Total	70.2M	2640

A cylindrical cut is used to remove redundant control volumes on the background grid in the region where the overset grids are located, keeping in mind overlap for interpolation (figure 5b). All surfaces have a minimum wall-normal spacing of $0.00083D_P$ with a growth ratio of 1.01. Like the open case, the propeller blades contain a pill-box of tetrahedral cells around them. On the blade surface, four prism layers are extruded while on the duct surface, four hexahedral layers are extruded all at an initial wall-normal height of $0.00083D_P$ and a growth ratio of 1.01. The tip gap region has an average spacing of $0.0083D_P$. More details can be found in Kroll and Mahesh (2022).

For statistical convergence of the unsteady loads and flow field in crashback, the ducted propeller is run for 234 revolutions and 150 revolutions of statistics are collected. The open propeller case is run for 300 revolutions and again 150 revolutions of statistics are collected. The computational time step used for both cases is $\Delta t U/D_P = 1.667 \times 10^{-4}$, which corresponds to a propeller rotation of 0.1286 degrees per time step. According to the experimental observations of Jessup et al. (2004), the force coefficients in crashback do not vary with Reynolds number in the range of $4 \times 10^5 < Re_D < 9 \times 10^5$. Table 6 summarizes the details for the crashback and VPWT cases studied in this paper.

Table 6: Details for the different cases simulated to study the VPWT geometry effects.

	<i>Empty VPWT</i>	<i>Open Prop VPWT</i>	<i>Ducted Prop VPWT</i>
<i>J</i>	-	-0.82	-0.82
<i>Re</i> _D	561,000	561,000	561,000

RESULTS

Bare Hull DARPA SUBOFF

The instantaneous flow field for the bare hull SUBOFF with the blowing trip is shown in figure 6, which shows instantaneous contours of *Q*-criterion (Hunt et al., 1988) colored by the instantaneous axial velocity. It is clear that the numerical blowing trip at $x/D_H = 0.75$ ($x/L = 0.0875$) is effective in transitioning the boundary layer, producing fine near-wall structures on the parallel mid hull region, which contribute to the hull drag. The deceleration of the boundary layer is apparent over the tapering stern, where the boundary layer thickens in the adverse pressure gradient and separates to form the wake.

Figure 7 shows the distribution of the circumferentially-averaged pressure coefficient and skin friction coefficient along the hull for the numerical blowing trip and the resolved trip wire. The pressure

coefficient is defined as

$$C_p = \frac{P - P_\infty}{\frac{1}{2}\rho U_\infty^2}, \quad (4)$$

where U_∞ and P_∞ are the free-stream velocity and pressure, respectively. The skin friction coefficient is defined as

$$C_f = \frac{\tau_w}{\frac{1}{2}\rho U_\infty^2}, \quad (5)$$

where τ_w is the shear stress at the wall. The simulation results are compared to the experimental measurements of Huang et al. (1992), which were conducted at $Re_L = 1.2 \times 10^7$, higher than the $Re_L = 1.1 \times 10^6$ of the present LES. Since C_p is relatively insensitive to Re for attached flows, we compare the numerical results directly to the experimental data in figure 7a. This plot demonstrates the good agreement between both simulation results and the experimental measurements. The numerical C_f cannot be compared directly to the experimental measurements of Huang et al. (1992) in figure 7b due to the difference in Reynolds number, so a scaling of the experimental data by $C_f \sim Re_L^{-1/5}$ is performed to compare to results at the present Re_L , which is valid for the zero pressure gradient mid hull. Again, the LES shows good agreement with experiments.

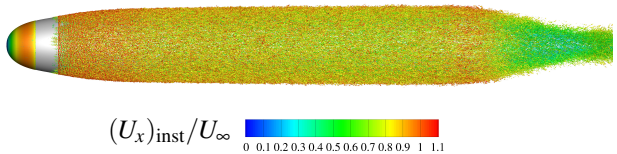


Figure 6: Instantaneous iso-contour of *Q*-criterion colored by instantaneous axial velocity for the bare hull tripped by numerical blowing.

Analysis of tripping effects

While the C_p on the hull surface of the resolved trip and numerical trip are nearly identical over most of the hull length, we note some local differences in the vicinity of the trip at $x/L \approx 0.0875$ in figure 7a. Both the blowing trip and the resolved trip wire produce a spike in pressure in front of the trip immediately followed by a sharp decrease in pressure over the trip. Interestingly, the blowing trip produces a larger pressure rise in front of the trip, but the separation bubble behind the resolved trip wire produces a much lower dip in pressure behind the trip than the blowing method. Figure 8 shows contours of mean velocity magnitude around the blowing trip and resolved tripwire along with streamlines. Examination of figure 8b reveals that the trip height is smaller than the upstream boundary layer thickness, and the trip causes a

deflection of the near-wall streamline around its blockage. While the blowing trip does produce a displacement of the near-wall streamline, it is not to the same extent as the tripwire, which creates a recirculation bubble that is an order of magnitude longer than the trip diameter. The corresponding contours of C_p in figure 9 demonstrate that this recirculation bubble is the source of the large dip in C_p behind the trip location in figure 7a. Another feature of the resolved tripwire is the pressure rise immediately after this dip of C_p in the recirculation bubble (as seen in figure 7b), which is not captured by the blowing trip. Figure 9b reveals that this increased pressure is due to the reattachment point at the tail of the recirculation bubble.

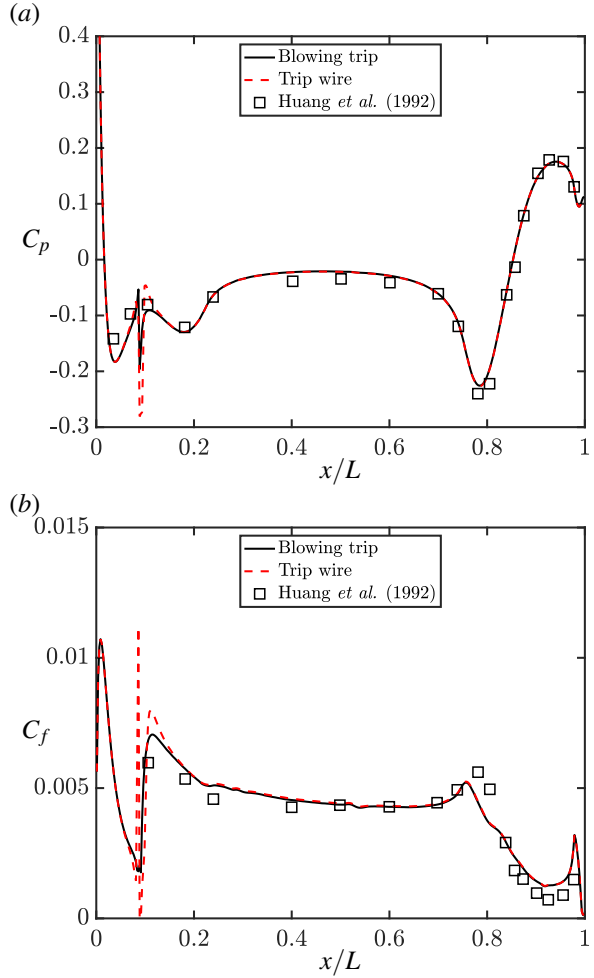


Figure 7: Contours of C_p and C_f along the hull surface compared to the experiments of Huang et al. (1992) at $Re_L = 1.2 \times 10^7$ (□) and the blowing trip LES of Morse and Mahesh (2021) (—). Note that $C_f \sim Re^{-1/5}$ scaling has been used to scale the experimental C_f measurements to the simulation Reynolds number.

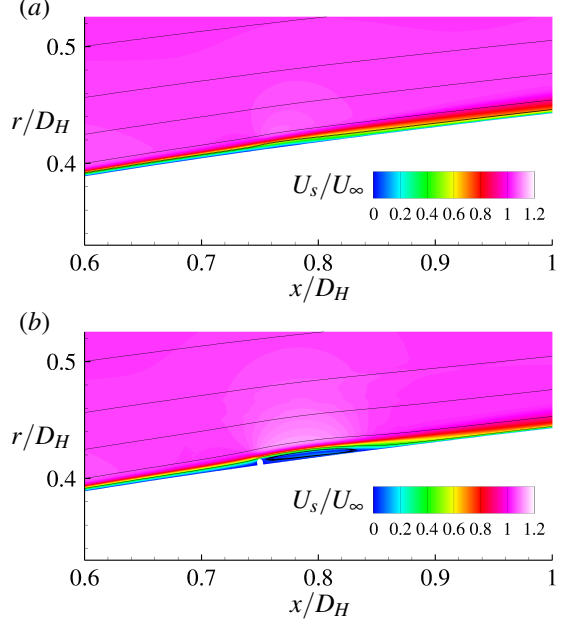


Figure 8: Contours of mean velocity magnitude and streamlines near the trip location for the numerical blowing trip (a) and the resolved trip wire (b).

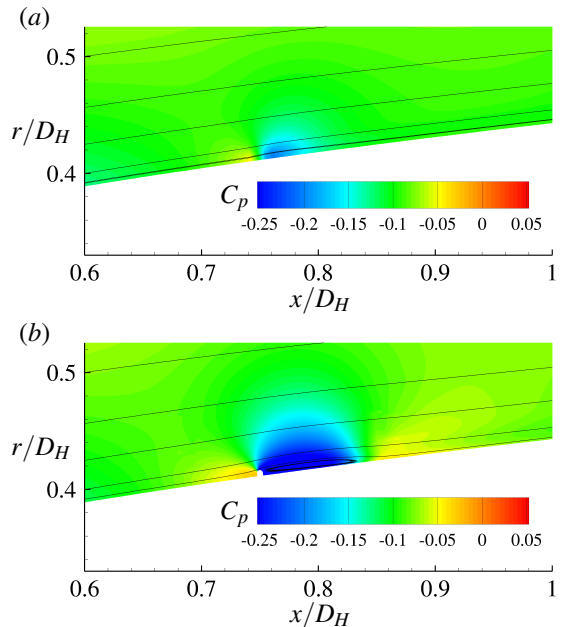


Figure 9: Contours of the mean pressure coefficient and streamlines near the trip location for the numerical blowing trip (a) and the resolved trip wire (b).

Examining the evolution of C_f along the hull (figure 7b), the blowing trip and resolved trip wire show large differences near the tripping location ($x/L \approx 0.0875$) and a small offset over the mid-hull, where the C_f of the

resolved trip is slightly higher. At the tripping location, there is a large spike in C_f over the trip, due to the acceleration of flow and local high shear over the top of the trip wire, as seen in figure 8b. After the recirculation bubble, the reattachment of the flow causes the resolved trip wire C_f to exceed the blowing trip C_f over $0.1 < x/L < 0.17$.

Figure 10 shows contours of the Reynolds shear stress $\overline{u_x u_r}$ and streamlines near the blowing and resolved trip. In figure 10a, there is a signature of some turbulence preceding the trip location at $x/D = 0.75$. On the other hand, contours of $\overline{u_x u_r}$ around the trip wire (figure 10b) show very low turbulence over most of the circulation bubble, followed by a large rise in $\overline{u_x u_r}$ approaching the reattachment point. To investigate this difference, figure 11 shows an iso-contour of instantaneous Q -criterion for both the blowing trip and the resolved tripwire. While both trips promote a quick transition of the boundary layer, the blowing trip promotes small turbulent spots ahead of the trip, which may be due to grid non-uniformity at the blowing location. On the other hand, the recirculation bubble shear layer behind the resolved trip is populated by quasi two-dimensional structures, which can be seen as red bands on top of the separation bubble in figure 11b. These structures rapidly break down and lose their span-wise coherence at the end of the circulation bubble, contributing to the large $\overline{u_x u_r}$ behind the resolved trip wire.

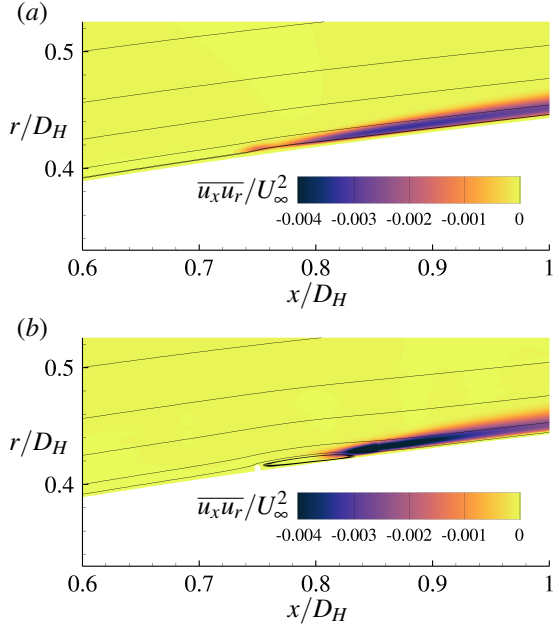


Figure 10: Contours of Reynolds shear stress and streamlines near the trip location for the numerical blowing trip (a) and the resolved trip wire (b).

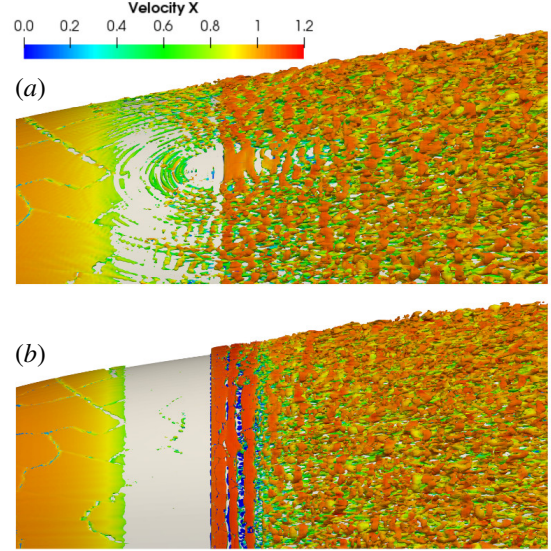


Figure 11: Iso-contour of instantaneous Q -criterion colored by instantaneous axial velocity for the numerical blowing trip (a) and the resolved trip wire (b).

The flat-plate boundary layer momentum integral equation is given by

$$\frac{1}{2}C_f = \frac{d\theta}{dx} + \frac{\theta}{U_e}(H+2)\frac{dU_e}{dx}, \quad (6)$$

where H is the shape factor and U_e is the edge velocity of the boundary layer. The second term on the right-hand side is eliminated for a zero-pressure gradient boundary layer, leaving an equation which may be integrated to obtain

$$\theta(x) = \theta(x_{\text{trip}}) + \Delta\theta + \frac{1}{2} \int_{x_{\text{trip}}}^x C_f dx', \quad (7)$$

where $\theta(x_{\text{trip}})$ is the momentum thickness of the laminar boundary layer at the tripping location, x' is the integration variable for x , and $\Delta\theta = D_{\text{trip}}/\rho U_\infty^2$ is the increase in momentum thickness across the trip, where D_{trip} is the drag on the trip per unit span. Preston (1958) suggests that the two functions of a trip are to provide a suitable perturbation and produce a $\Delta\theta$ to bring Re_θ above the minimum value required for a turbulent boundary layer. Note that the collapse of C_f after a short distance downstream of the trip (figure 7b) suggests that the percent difference in θ between the two cases diminishes at long distances downstream of the trip, as long as the integral of C_f along x dominates the local differences in θ and C_f near the trip.

To investigate the persisting differences downstream of the trip, we compare profiles of the fully-developed turbulent boundary layers along the parallel mid-hull for the resolved trip wire and blowing

trip. Figure 12a shows profiles of mean axial velocity for positions $x/L = 0.28, 0.35, 0.42, 0.49$ downstream of the front of the hull, while figure 12b shows profiles of $\bar{u}_x \bar{u}_r$ at the same stations. The profiles are very similar between the two tripping methods, with the only apparent difference being an approximately 5 percent thicker boundary layer for the blowing trip method. This small difference may be due to the difference in $\Delta\theta$ produced across the trip or the slight delay in transition with the resolved trip (figure 10b).

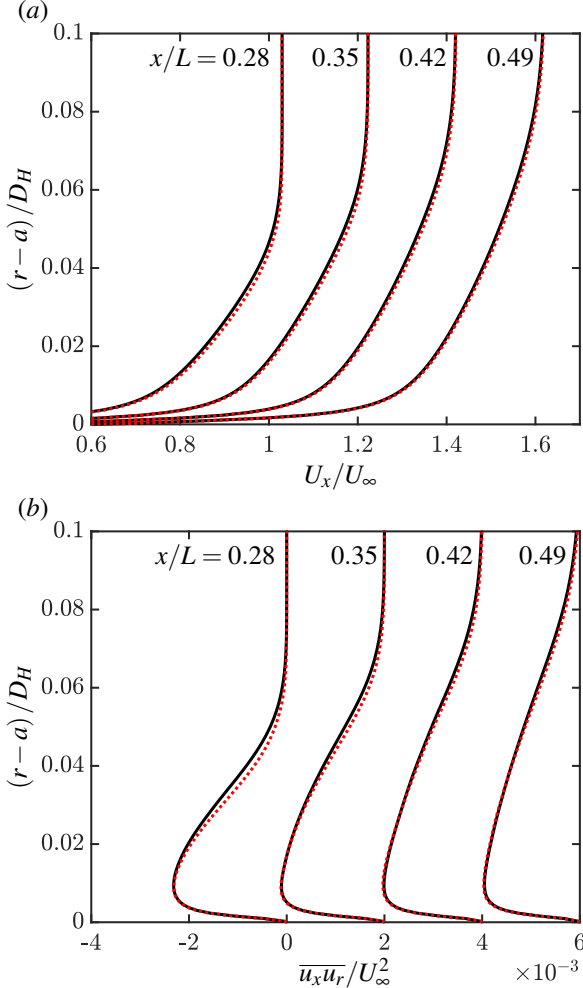


Figure 12: (a) Profiles of mean axial velocity at stations $x/D_H = 0.28, 0.35, 0.42, 0.49$ for the numerical blowing trip (—, black) and the resolved trip wire (· · · · ·, red). Note that successive profiles have been shifted horizontally by 0.2. (b) Corresponding profiles for $\bar{u}_x \bar{u}_r$, where successive profiles have been shifted horizontally by 0.002.

Overall, these results indicate that the blowing method is sufficient to produce a hull boundary layer with satisfactory quantitative agreement with a boundary layer

produced by resolving the experimental trip geometry. This is encouraging given the lower computational cost of the blowing trip, although more computations with different blowing rates are required to completely characterize the blowing trip method. However, this result relies on the criteria of Schlatter and Örlü (2012) that transition is initiated within the boundary layer and it is not over or under tripped. Therefore, it must be noted that this result is specific to the placement and sizing of this specific trip geometry, and different outcomes may be expected for larger experimental trips, such as that of the appended SUBOFF (Jiménez et al., 2010b).

Analysis of streamline curvature

We now focus on insights into the streamline curvature from LES of the bare hull with the blowing trip from Morse and Mahesh (2021). Morse and Mahesh (2021) proposed an alternative method of analyzing turbulent boundary layers with curvature by deriving the streamwise and streamwise-normal mean momentum equation for axisymmetric streamline coordinates, simplified using the boundary layer approximation as

$$U_s \frac{\partial U_s}{\partial s} = -\frac{1}{\rho} \frac{\partial P}{\partial s} - \frac{1}{r} \frac{\partial}{\partial n} \left(r \bar{u}_s \bar{u}_n - r v \frac{\partial U_s}{\partial n} \right), \quad (8)$$

$$\frac{U_s^2}{R_s} = -\frac{1}{\rho} \frac{\partial P}{\partial n} - \frac{1}{r} \frac{\partial}{\partial n} \left(\bar{u}_n^2 \right). \quad (9)$$

In these equations, s is the streamwise coordinate direction, n is the streamwise-normal coordinate direction, and $U_s + u_s$, u_n , and u_θ are the total (mean plus fluctuating) velocities in the s , n , and θ directions, respectively. Additionally, R_s is the curvature of streamlines, defined as

$$\frac{1}{R_s} = \frac{1}{U_s} \left(\Omega + \frac{\partial U_s}{\partial n} \right), \quad (10)$$

where Ω is the sole component of mean vorticity (in the θ direction). This definition means that the U_s^2/R_s term on the left-hand side of the streamline-normal momentum equation (9) represents the mean centripetal acceleration of fluid elements along streamlines.

The streamline coordinate formulation of the mean momentum equations has several benefits, which Morse and Mahesh (2021) discuss in detail. First, the total stress on the right-hand sides of equation 8 and the Reynolds stress on the right-hand side of equation 9 go to zero outside of the boundary layer, producing the differential form of Bernoulli's equation and Euler's equation for curved streamlines. Another useful property is that the streamline-normal coordinate is normal to wall boundaries, while also being normal to the free-stream velocity far from the body, simplifying analysis and

allowing for boundary layer approximations for curved bodies with thick boundary layers. Finally, an additional benefit of the streamline coordinates is the direct inclusion of the streamline curvature term in equation 9 for the streamwise-normal mean momentum.

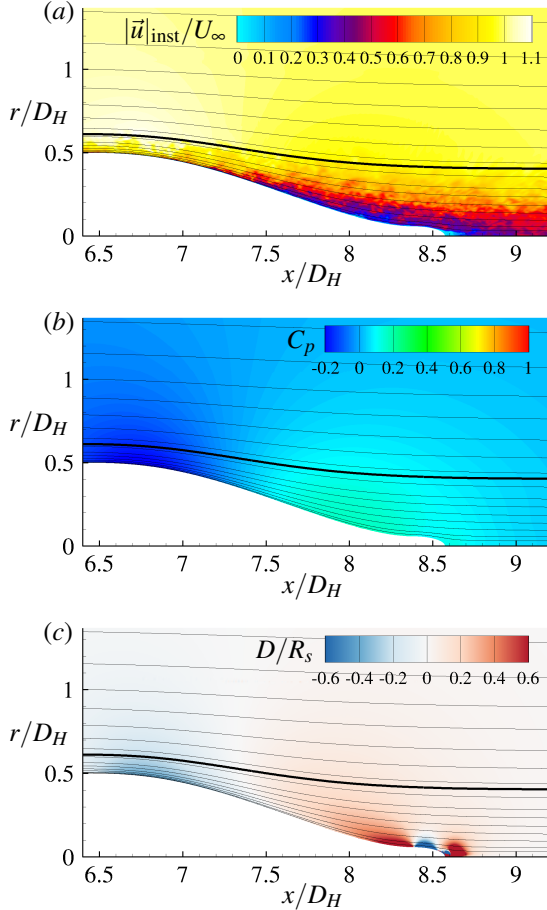


Figure 13: Contours of instantaneous velocity magnitude (a), mean pressure coefficient (b), and normalized mean streamline curvature (c) along the stern of the bare hull from Morse and Mahesh (2021). The edge of the boundary layer is shown as a bold black line, while thin black lines represent streamlines.

Figure 13 shows contours of the instantaneous velocity magnitude, mean C_p , and normalized streamline curvature at the stern of the bare hull. The thick boundary layer, as shown by the bold black line in figure 13, quickly grows at the stern, and it is apparent that the pressure varies normally from the wall in figure 13b. This is due to the streamline curvature inside the boundary layer, which is visualized in figure 13c.

Using equations 8 and 9 it is possible to formulate simple expressions for the pressure coefficient at the wall and the pressure difference between the wall

and the boundary layer edge. These expressions are

$$C_p = 1 + \frac{2}{U_\infty^2} \int_0^\infty U_s \Omega dn, \quad (11)$$

$$P_w - P_e = \frac{1}{2} \rho U_e^2 + \rho \int_0^\delta U_s \Omega dn, \quad (12)$$

where P_w is the pressure at the wall, P_e is the pressure at the boundary layer edge, and δ is the boundary layer thickness. Note that Ω is the mean vorticity so the integral of $U_s \Omega$ converges outside the boundary layer. Figure 14 shows the right-hand and left-hand sides of equation 12 calculated from the bare hull LES. The left-hand side term is calculated directly from the pressure difference between the wall and the boundary layer edge, while the right-hand side is evaluated by integrating the simulated mean flow field along streamline-normal lines away from the wall. From the figure, it is first apparent that left-hand and right-hand sides of equation 12 are in very good agreement. Secondly, it is clear that P_w and P_e are identical over the parallel mid hull, which is expected using the typical boundary layer approximations. We see that over the stern, the streamline curvature term (which appears through Ω in equation 12) causes P_w to dip below P_e for the area of convex curvature, while the opposite is true for the concave curvature near the end of the stern.

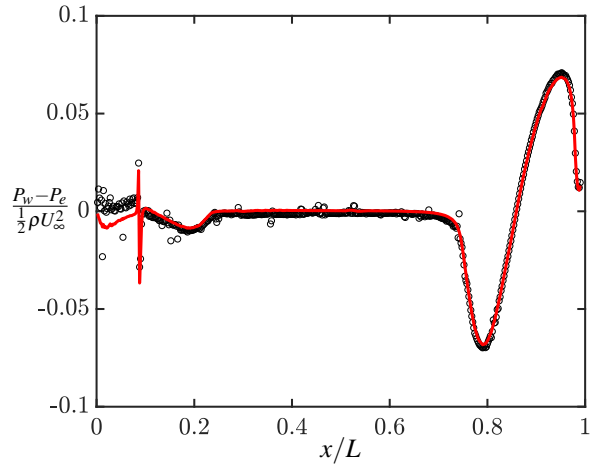


Figure 14: Left-hand (—, red) and right-hand (○) terms of equation 12 non-dimensionalized by $\frac{1}{2} \rho U_\infty^2$, showing the pressure difference between the wall and the edge of the boundary layer (Morse and Mahesh, 2021).

Appended DARPA SUBOFF

Wall-resolved LES of the appended SUBOFF was performed at $Re_L = 1.2 \times 10^6$ with various tripping configurations. A visualization of the instantaneous flow field around the appended hull with the resolved tripwire is shown in figure 15, which shows an instantaneous

iso-contour of Q -criterion colored by axial velocity. The large blockage of the hull trip wire is apparent, with the boundary layer thickening rapidly in the wake of the wire. Moving downstream along the hull, the transitional flow on the sail is apparent in this configuration without the appendage trips. Near the end of the hull, the stern appendages are barely visible, as much of their area is immersed in the thick stern boundary layer.

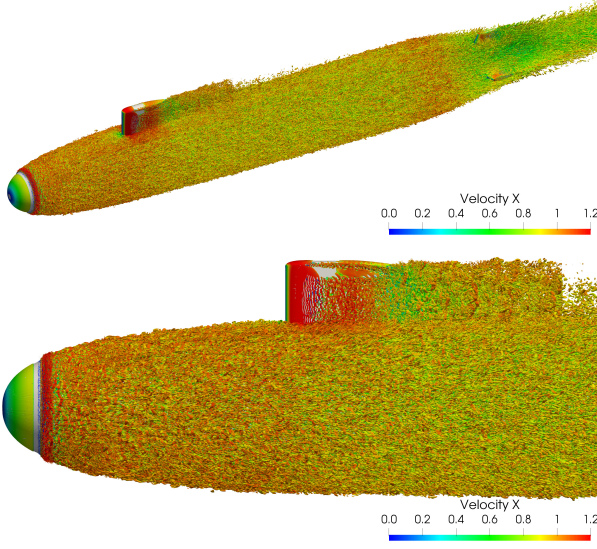


Figure 15: Iso-contour of instantaneous Q -criterion colored by axial velocity for the appended hull with the resolved hull trip wire.

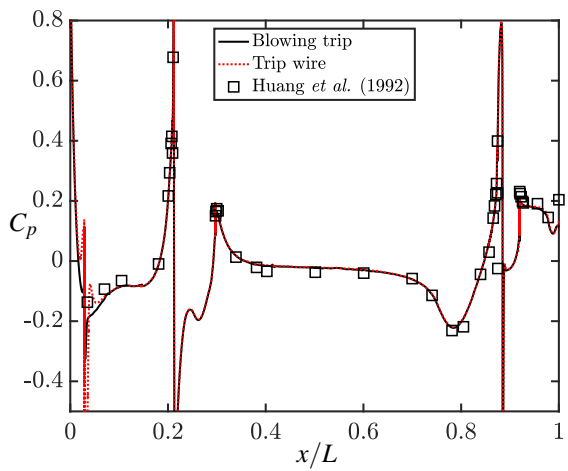


Figure 16: Distribution of C_p along the hull surface along the upper meridian line (a). The experimental data of Huang et al. (1992) at $Re_L = 1.2 \times 10^7$ is shown as symbols.

Figure 16 shows the distribution of the pressure coefficient on the hull surface for the blowing trip compared to the resolved trip wire and the experiments of Huang et al. (1992). In particular, figure 16 shows the pressure along the upper meridian through the sail and upper stern appendage. The pressure coefficient from LES shows good agreement with the experimental data, even near the stagnation points around the sail and stern appendage. The flow stagnation produced by the trip wire produces a large rise in C_p in front of the trip wire and actually eliminates the small region of suction in front of the trip from the blowing trip calculation. The acceleration of the flow over the trip wire causes a spike in negative C_p on top of the wire, followed by a large region of negative C_p in the recirculation bubble behind the trip wire. The reattachment behind the separation bubble induces a spike in pressure that is not observed for the blowing trip. After the pressure recovers from this spike, there is no discernible difference in C_p between the resolved trip wire and blowing trip for $x/L > 0.075$. Further computations and statistics analysis will investigate in detail the effect of this trip wire configuration, which is expected to differ from the bare hull due to the larger trip diameter. Since this trip is larger than the local boundary layer thickness, the analysis of Schlatter and Örlü (2012) would indicate that there may be persistent effects from the trip wire far downstream of the tripping location.

Next, we focus on the effect of tripping on the appendages. Figure 17 shows the pressure coefficient along the sail compared to the experimental measurements of Huang et al. (1992) at $Re_L = 1.2 \times 10^7$. Kroll et al. (2020) previously reported the same quantity along the sail, showing good agreement with experiments except at around 25 percent chord (the location of the third experimental measurement point). From the current LES in figure 17, it is apparent that tripping at 5 percent chord to emulate the Huang et al. (1992) experiments results in a substantial improvement in the agreement of C_p for all sail spanwise locations. This improvement is attributed to the fixed transition point, as opposed to the natural transition that occurs for the LES results without the trip.

Figure 18 shows similar profiles of C_p along the upper stern appendage at 10 and 50 percent of the appendage height compared to the data of Huang et al. (1992) at $Re_L = 1.2 \times 10^7$. Examining the distribution of C_p along the stern appendage, we can see that the effect of tripping is smaller than what was observed for the sail, and the agreement with experiments is good for both the tripped and non-tripped LES. This may be due to the location of the stern appendages, which are primarily within the thick stern boundary layer. In particular, this upper stern appendage is also in the wake of the sail.

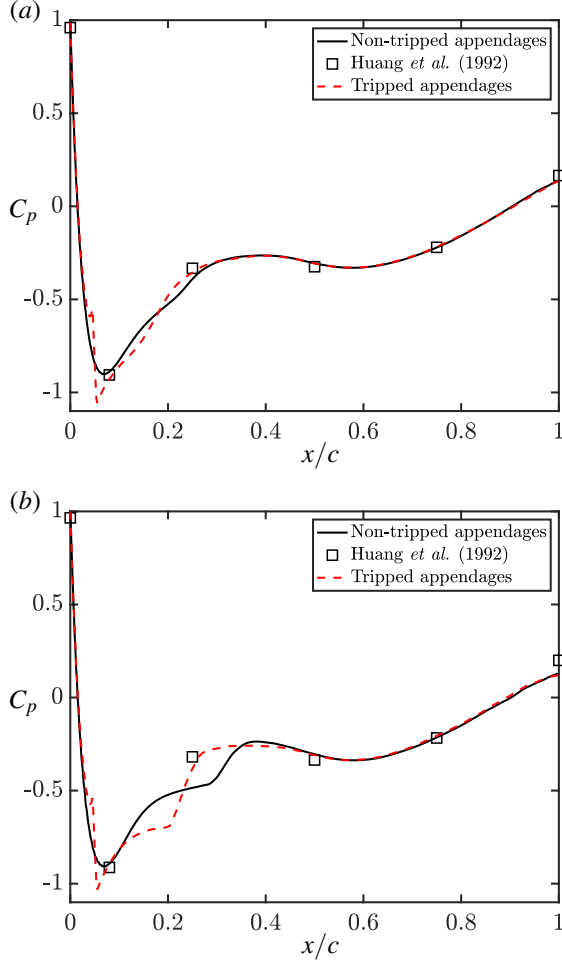


Figure 17: Pressure coefficient along the sail at stations at 10 percent (a) and 50 percent (b) of the sail height compared to the experiments of Huang et al. (1992) for LES with and without tripping. The x -coordinate has been normalized by the sail chord, c .

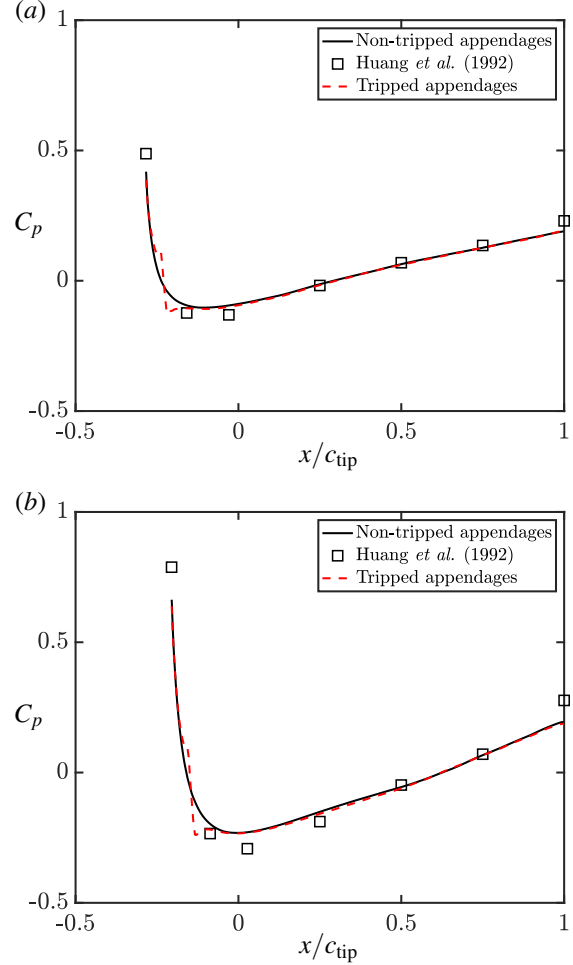


Figure 18: Pressure coefficient along the top stern appendage at stations at 10 percent (a) and 50 percent (b) of the sail height compared to the experiments of Huang et al. (1992). The x -coordinate has been normalized by the stern appendage tip chord, c_{tip} . LES results without tripping and with tripping at 5 percent chord are shown.

36-inch Variable Pressure Water Tunnel

Figure 19a,b shows contours on the $z = 0$ plane, on which we can identify the different flow features in the open jet section of the VPWT. Upstream, flow is accelerated until the tunnel outlet nozzle, where the tunnel free-stream velocity U_∞ is achieved and remains constant throughout the propeller center location. The most noticeable flow feature is the free shear layer formed as the tunnel outlet interacts with the plenum chamber of the open jet (figure 19a). The shear layer produces some vortices and unsteadiness is introduced to the flow (figure 19b). Away from the shear layer and towards the test-section center, the flow is uniform throughout, as designed. Downstream, flow is funneled out of the test section and a higher pressure region is observed in figure 19b, as flow collides with the collector walls.

When studying design condition propeller flows in a closed jet water tunnel, confinement effects can be reduced by minimizing the ratio η :

$$\eta = A/C, \quad (13)$$

where A is the propeller cross-sectional area and C is the area of the test section. It is suggested that $\eta \ll 1$ to avoid confinement (Glauert, 1935; Barlow et al., 1999). We can calculate $\eta = 0.11$ for our case, using the radius of $1.5D_P$ from the test section center to the shear layer. However, the use of an open jet in the VPWT further reduces any confinement effects to a small fraction that of a closed tunnel of the same C and these effects are negligible for the forward mode case, where the wake is of a similar size as the propeller diameter since there is

no ring vortex. There are theoretical corrections to the confined data proposed in literature. Although Glauert (1935) introduced linearized corrections for a propeller in the forward mode of operation, in crashback there are no known theoretical corrections.

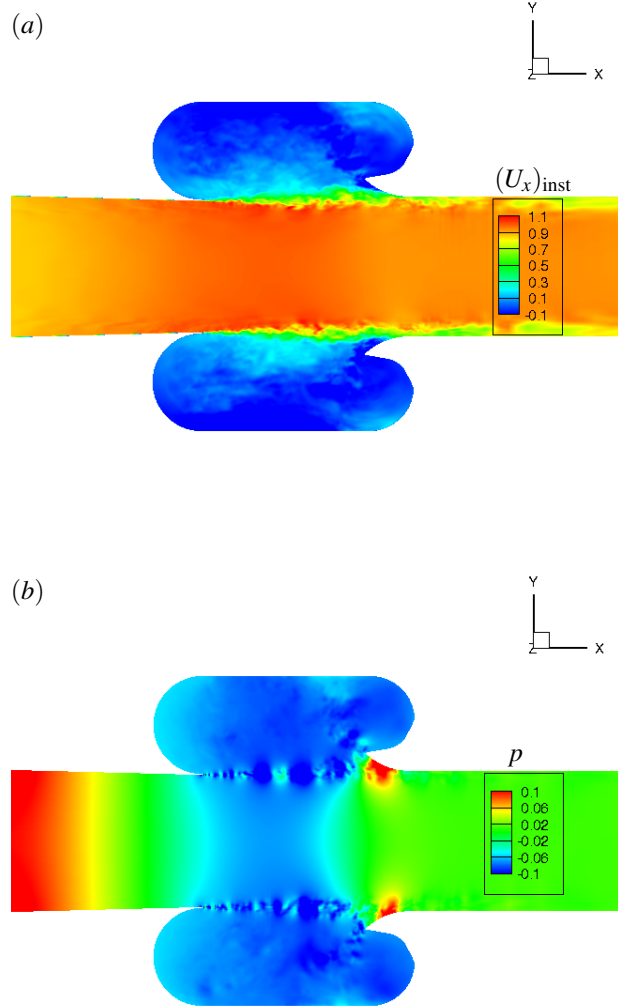


Figure 19: Constant $z = 0$ plane contours of (a) instantaneous axial velocity $(U_x)_{\text{inst}}$ and (b) instantaneous pressure p . The flow field quantities are normalized with ρ and U_∞ .

Open Propeller Crashback ($J=-0.82$)

The propeller loads are of great interest during a crashback maneuver as the unsteadiness of the vortex ring can have a major effect on increasing their magnitude and produce high standard deviations. The side-force K_s is especially important as it can negatively impact the

maneuverability of a marine vehicle. Numerous previous publications (Výšohlid and Mahesh, 2006; Chang et al., 2008; Jang and Mahesh, 2013) validated their results for propeller P4381 in an open configuration by comparing loads to the experiments (Jessup et al., 2004, 2006). When trying to validate computational results, the propeller load statistics showed a deviation from the experimental results, more specifically for K_T and K_Q . Some of these results are compared at $J = -0.7$ in table 7, where K_T and K_Q for LES results differ greatly from those in the VPWT. They match better to experiments done in an open water setting, suggesting that confinement effects could be a factor for the differences in the loads.

Table 7: Crashback $J = -0.7$: Statistics of unsteady loads for LES compared to experiments. LES-1 (Jang and Mahesh, 2013), LES-2 (Kroll et al., 2020), VPWT (Jessup et al., 2004), and OW (Ebert et al., 2007).

	$\langle K_T \rangle$	$\langle K_Q \rangle$	$\langle K_S \rangle$
LES-1 (Coarse)	-0.39	-0.078	0.035
LES-1 (Fine)	-0.38	-0.074	0.027
LES-2	-0.41	-0.081	0.029
VPWT	-0.33	-0.065	0.030
OW	-0.41	-0.078	-

The VPWT Confinement Effects

The present LES results show that the VPWT geometry has major effects on the flow field (figure 20). The instantaneous axial velocity contours reveal that the unsteady vortex ring interacts with the tunnel outlet shear layer (figure 20a). As a result, flow downstream of the propeller interacts with the collector section of the VPWT, sometimes pushing flow into the plenum chamber of the open jet section. The mean axial velocity contours in figure 20(b) shows that the vortex ring and shear layer interaction results in a convex expansion effect moving towards the plenum chamber of the VPWT. However, the edge of the shear layer acts almost as a wall boundary, restraining flow from moving further outwards. The effect of the vortex ring is similar to that of a bluff body, leading to what is known as a solid blockage effect (Barlow et al., 1999). Blockage interference is the result of the displacement of streamlines around a model. More specifically, solid blockage is the contribution due to the displacement of the model volume inside the water tunnel. For an open jet water tunnel, this causes the tunnel jet boundary to expand as visualized in figure 20(b). The effect of the vortex ring is therefore similar to that of a bluff body.

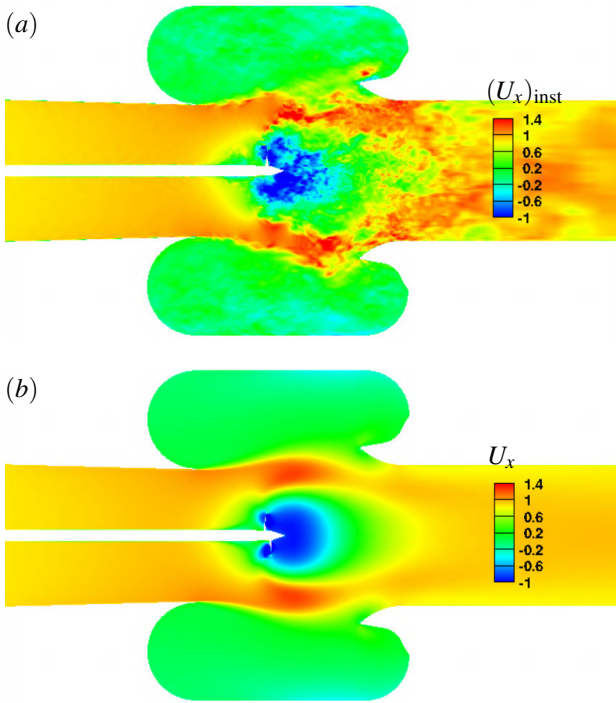


Figure 20: Crashback $J = -0.82$: $z = 0$ plane contours of (a) instantaneous axial velocity $(U_x)_{\text{inst}}$ and (b) mean axial velocity U_x . The flow field quantities are normalized with U_∞ .

The solid blockage effect for open jet water tunnels is referred to as the jet-expansion effect which tends to decrease the effective velocity experienced by the model. This is because the increased cross-sectional area of the tunnel shear layer would require a decrease in the flow velocity due to continuity. The relevant parameter to assess solid blockage is the ratio of model cross-sectional area to the tunnel flow cross-section area or η (Barlow et al., 1999). An important insight from this case is that the vortex ring diameter at minimum should replace the propeller diameter as the relevant length scale, as it acts as a blockage to the tunnel flow around it. As a result, the true blockage is much higher than what the η based on the propeller cross-sectional area would indicate. Although the edge of the shear layer expands in size, it is not enough to reduce η and prevent blockage effects.

Solid blockage in the VPWT for the crashback case has a direct effect on the advance ratio J and thus the propeller loads. The reduced flow velocity results in a reduced effective J magnitude due to its relationship to the free-stream velocity, $|J| \propto U_\infty$. Therefore, for any prescribed J in the VPWT, the resulting flow field is effectively that of a lower magnitude J in an unconfined case. This is the reason K_T and K_Q from the VPWT experiments is lower in magnitude compared to

open water (OW) and unconfined LES results in table 7, following the trend from the crashback load data presented in Jessup et al. (2004, 2006).

After including the VPWT geometry in the LES crashback simulation, the resulting load statistics match the experiments better as K_T and K_Q are within 5% of the VPWT experiments (table 8). This result suggests the inclusion of the VPWT geometry is required for validation in order to properly match the experimental boundary conditions. For a ducted propeller in crashback, the vortex ring diameter is larger and closer to the tunnel shear layer. This is the reason it was essential that Kroll and Mahesh (2022) include the VPWT geometry to validate the ducted case.

Table 8: Crashback $J = -0.82$: Statistics of unsteady loads for LES compared to experiments in the VPWT (Jessup et al., 2004).

	$\langle K_T \rangle$	$\sigma(K_T)$	$\langle K_Q \rangle$	$\sigma(K_Q)$	$\langle K_S \rangle$
Present	-0.39	0.056	-0.076	0.011	0.028
VPWT	-0.38	-	-0.073	-	0.031

Ducted Propeller Crashback ($J=-0.82$)

The instantaneous flow in figure 21(a,b) shows that the unsteady vortex ring is bigger than in figure 20 and interacts with the tunnel outlet shear layer pushing flow into the plenum chamber of the open jet section even further than the open propeller result. The area between the model and tunnel shear layer is reduced even further, increasing blockage effects. The result is the lack of a uniform, free-stream flow around the vortex ring as would be expected in an open water setting. Overall, these tunnel effects result in a flow field and vortex ring behavior that might not exactly occur in an open water environment. However, for validation and a better comparison of the simulation to the experiment, the VPWT geometry should be considered and included.

It is important to understand the mechanisms behind the highest K_S which could negatively impact maneuverability. It was shown from previous experiments and LES (Swithenbank et al., 2008; Donnelly et al., 2010; Jang and Mahesh, 2012) that the mean side-force for the ducted propeller is higher in magnitude compared to an open propeller due to the addition of the ducted geometry. Kroll and Mahesh (2022) reported in detail the validation and insights gained from the LES of a ducted propeller in crashback with the VPWT geometry included. Figure 22 shows the force history of the force coefficients summed on all surfaces, which shows high fluctuations of the force coefficients. Most importantly, the K_S magnitude can vary immensely at times and potentially lead to unpredictable effects on maneuverability. The highest side-force magnitude fluctuations were found to be related

to the stability of the vortex ring. The use of LES helps capture the unsteady vortex ring shedding events that produce the highest loads (figure 23).

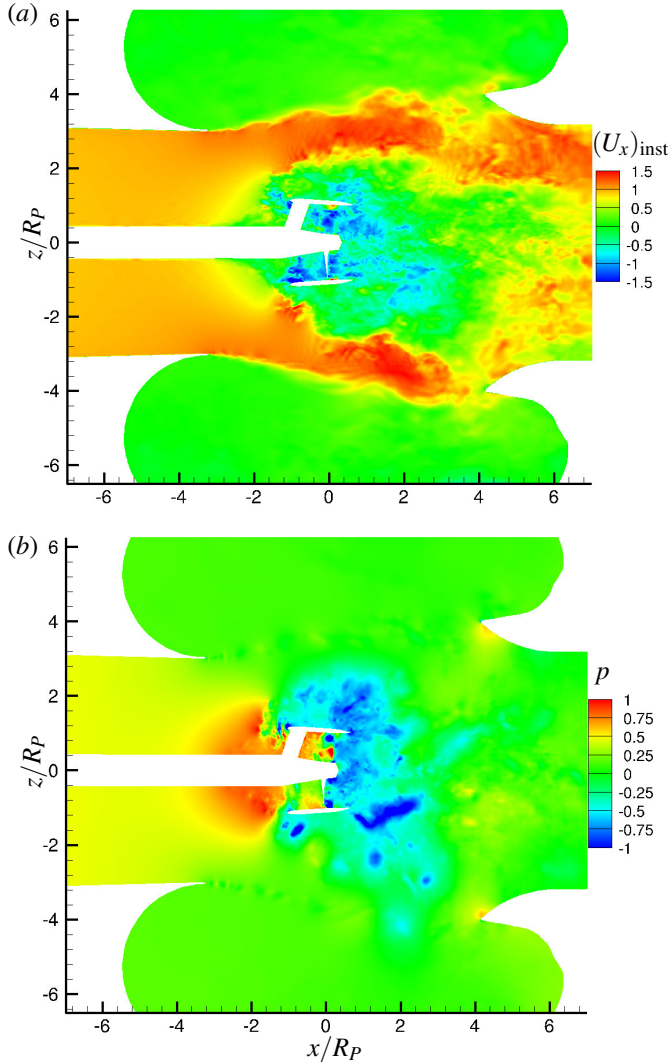


Figure 21: The instantaneous flow field for crashback of a ducted propeller at $J = -0.82$. (a) Instantaneous axial velocity $(U_x)_{\text{inst}}$ contour at the constant y -plane slice at $y = 0$ (Kroll and Mahesh, 2022). Note the acceleration of the flow around the vortex ring and the shear layer expansion into the plenum chamber of the VPWT. (b) The pressure field p contour at the constant y -plane slice $y = 0$. Upstream of the duct is a high pressure region as the forward-moving flow is slowed down by the propeller reverse flow. Low pressure regions representing vortices are observed. The axes are normalized with the propeller radius $R_P = D_P/2$. The flow field quantities are normalized with ρ and U_∞ .

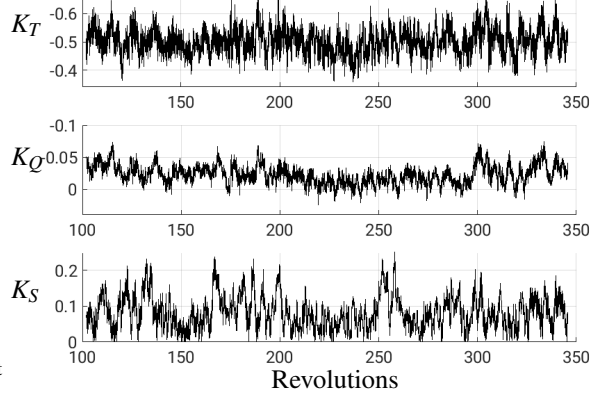


Figure 22: A total of 234 revolutions of the unsteady load history of the force coefficients K_T , K_Q and K_S summed from all surfaces (blades, duct, stator blades, and hub).

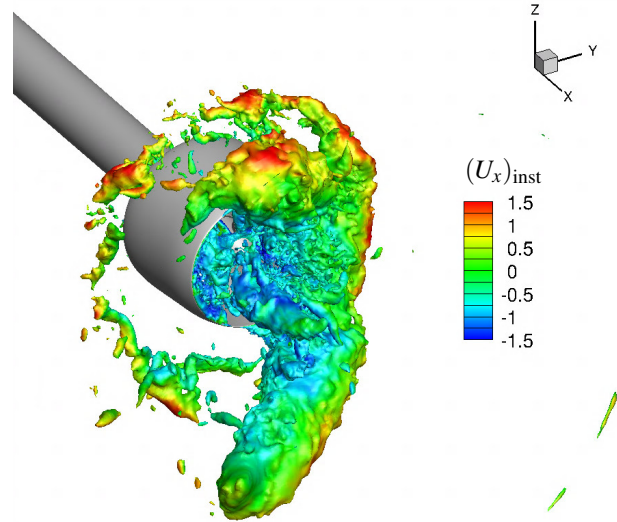


Figure 23: The instantaneous flow field showing iso-contour of pressure $p = -0.70$ colored by the axial velocity $(U_x)_{\text{inst}}$ (Kroll and Mahesh, 2022). An incoherent, broken down vortex ring during a shedding event. The flow field quantities are normalized with ρ and U_∞ .

Jang and Mahesh (2012) showed that the large pressure gradients inside the duct produce a flow between the rotor blade tips and the duct surface in the small tip gap called tip-leakage flow. Kroll and Mahesh (2022) showed that the tip-leakage flow for this case is strong enough to create blade-local recirculation zones which rotate with each of the 5 propeller blades. Tip-leakage flow and these blade-local recirculation zones were found to play a crucial role in creating high fluctuations in K_S . Interestingly, Kroll and Mahesh (2022) also showed

that the largest fluctuations in K_S are locally linked to the downstream, sharp leading edge of the duct. This is because the unsteady, propeller induced reverse flow collides with the sharp leading edge at variable, high angles of attack creating separated flow. This conclusion is supported by the fact that the highest local mean K_S comes from the most downstream segment of the duct, associated with the sharp leading edge.

SUMMARY AND FUTURE WORK

Overset large-eddy simulation was used to explore several problems of interest for submerged marine vehicles. This work has a particular focus on matching experimental boundary conditions, such as tripping and water tunnel geometry confinement effects, in order to validate the simulation results. The use of the overset method allowed for the trip geometry and confinement due to the water tunnel geometry to be explored systematically without requiring recreation of meshes around the propeller or hull model. Leveraging this flexibility greatly reduced simulation turnaround time and provided better validation comparison to the experiments.

The use of a resolved trip wire and numerical blowing were contrasted for the bare hull DARPA SUBOFF and appended DARPA SUBOFF. It was found that the numerical blowing method is satisfactory in producing a turbulent hull boundary layer for the bare hull case. However, there are some local differences near the vicinity of the trip location. A separation bubble and a reattachment point are observed behind the resolved trip. Further computations are focused on assessing the downstream effects of the larger appended SUBOFF trip wire. Simulations of the appended SUBOFF with tripped appendages demonstrated better agreement than was observed by Kroll et al. (2020). Streamline coordinate analysis the LES data of flow over the bare hull SUBOFF revealed the source of pressure variation within the stern boundary layer using the streamline momentum equations derived by Morse and Mahesh (2021).

For both the open and ducted propellers in crashback, the present LES revealed that it is important to include the VPWT geometry and its confinement effects to validate computational results. A solid blockage effect was found to be responsible for the discrepancies previously observed between VPWT and OW K_T and K_Q results. Capturing the unsteady side-forces for a ducted propeller in crashback helped to provide insight on the mechanisms behind their production. Kroll and Mahesh (2022) found these sources to be the vortex ring stability as well as leading edge separation and tip-leakage flow on the duct geometry.

ACKNOWLEDGEMENT

This work is supported by the United States Office of Naval Research (ONR) under ONR grant N00014-18-1-2356 with Dr. Ki-Han Kim as technical monitor. Computing resources for the present work were provided by the US Army Engineer Research and Development Center (ERDC) in Vicksburg, Mississippi, on the Onyx supercomputer of the High Performance Computing Modernization Program (HPCMP) and the Minnesota Supercomputing Institute (MSI) at the University of Minnesota.

REFERENCES

- Barlow, J., Rae, Jr. W. H., and Pope, A. Low-speed wind tunnel testing. John Wiley & Sons, 1999.
- Chang, P., Ebert, M., Young, Y. L., Liu, Z., Mahesh, K., Jang, H., and Shearer, M. “Propeller forces and structural responses to crashback”. In Proceedings of the 27th Symposium on Naval Hydrodynamics, Seoul, Korea, 2008.
- Chase, N. and Carrica, P. M. “Submarine propeller computations and application to self-propulsion of DARPA Suboff”. Ocean Engineering, 60:68–80, 2013.
- Chen, B. and Stern, F. “Computational fluid dynamics of four quadrant marine propeller flow”. Journal of Ship Research, 43:4:218, 1999.
- Davoudzadeh, F., Taylor, L. K., Zierke, W. C., Dreyer, J. J., McDonald, H., and Whitfield, D. L. “Coupled Navier–Stokes and equations of motion simulation of submarine maneuvers, including crashback”. In Proceedings of the 1997 ASME Fluids Engineering Division Summer Meeting, New York, 1997.
- Donnelly, M., Jessup, S., and Etebari, A. “Measurement of steady and unsteady duct loads for propeller 4381 at crashback conditions in the 36” water tunnel”. Technical Report NSWCCD-50-TR-2010/051, Naval Surface Warfare Center Carderock Division Hydromechanics Department Report, 2010.
- Ebert, M., Chang, P., and Mulvihill, L. “NSWCCD FY07 Crashback Computational Effort”. In 2007 ONR Propulsor S & T Program Review, October, 2007.
- Germano, M., Piomelli, U., Moin, P., and Cabot, W. H. “A dynamic subgrid-scale eddy viscosity model”. Physics of Fluids A, 3:7:1760, 1991.
- Glauert, H. Airplane Propellers. In: Aerodynamic Theory, volume 4. Springer, 1935.

- Horne, W. J. and Mahesh, K. “A massively-parallel, unstructured overset method for mesh connectivity”. *Journal of Computational Physics*, 376:585–596, 2019a.
- Horne, W. J. and Mahesh, K. “A massively-parallel, unstructured overset method to simulate moving bodies in turbulent flows”. *Journal of Computational Physics*, 397:108790, 2019b.
- Horne, W. J. and Mahesh, K. “A hardware accelerated unstructured overset method to simulate turbulent fluid flow”. *Journal of Computational Physics*, 444:110574, 2021.
- Huang, T., Liu, H. L., Groves, N., Forlini, T., Blanton, J., and Gowing, S. “Measurements of flows over an axisymmetric body with various appendages in a wind tunnel: the DARPA SUBOFF experimental program”. In *Proceedings of the 19th Symposium on Naval Hydrodynamics*, 1992.
- Hunt, J. C. R., Wray, A. A., and Moin, P. “Eddies, streams, and convergence zones in turbulent flows”. Center for Turbulence Research Report CTR-S88, page 193, 1988.
- Jang, H. and Mahesh, K. “Large eddy simulation of crashback in ducted propulsors with stator blades”. In *Proceedings of the 29th Symposium on Naval Hydrodynamics, Gothenburg, Sweden*, 2012.
- Jang, H. and Mahesh, K. “Large eddy simulation of flow around a reverse rotating propeller”. *Journal of Fluid Mechanics*, 729:151–179, 2013.
- Jessup, S., Chesnakas, C., Fry, D., Donnelly, M., Black, S., and Park, J. “Propeller performance at extreme off design conditions”. In *Proceedings of the 25th Symposium on Naval Hydrodynamics, St. John’s, Canada*, 2004.
- Jessup, S., Fry, D., and Donnelly, M. “Unsteady propeller performance in crashback conditions with and without duct”. In *Proceedings of the 26th Symposium on Naval Hydrodynamics, Rome, Italy*, 2006.
- Jiang, C. W., Dong, R. R., Lui, H. L., and Chang, M. S. “24-inch water tunnel flow field measurements during propeller crashback”. In *Proceedings of the 21st Symposium on Naval Hydrodynamics*. The National Academies Press, Washington DC, 1997.
- Jiménez, J., Hoyas, S., Simens, M. P., and Mizuno, Y. “The intermediate wake of a body of revolution at high reynolds numbers”. *Journal of Fluid Mechanics*, 659:516–539, 2010a.
- Jiménez, J. M., Reynolds, R. T., and Smits, A. J. “The effects of fins on the intermediate wake of a submarine model”. *Journal of Fluids Engineering*, 132(3):031102, 2010b.
- Kim, S.-E., Rhee, B. J., and Miller, R. W. “Anatomy of turbulent flow around DARPA SUBOFF body in a turning maneuver using high-fidelity RANS computations”. *International Shipbuilding Progress*, 60(1):207–231, 2013.
- Kroll, T., Morse, N., Horne, W., and Mahesh, K. “Large eddy simulation of marine flows over complex geometries using a massively parallel unstructured overset method”. In *Proceedings of the 33rd Symposium on Naval Hydrodynamics, Osaka, Japan*, 2020.
- Kroll, T. B. and Mahesh, K. “Large-eddy simulation of a ducted propeller in crashback”. *Flow*, 2:E-4, 2022. doi: 10.1017/flo.2021.18.
- Kumar, P. and Mahesh, K. “Large eddy simulation of propeller wake instabilities”. *Journal of Fluid Mechanics*, 814:361–396, 2017.
- Kumar, P. and Mahesh, K. “Large-eddy simulation of flow over an axisymmetric body of revolution”. *Journal of Fluid Mechanics*, 853:537–563, 2018.
- Lilly, D. K. “A proposed modification of the Germano subgrid-scale closure model”. *Physics of Fluids A*, 4:3:633, 1992.
- Liu, H. L. and Huang, T. “Summary of darpa suboff experimental program data”. Technical Report CRDKNSWC/HD-1298-11, *Naval Surface Warfare Center, Carderock Division (NSWCCD)*, 1998.
- Mahesh, K., Constantinescu, G., and Moin, P. “A numerical method for large-eddy simulation in complex geometries”. *Journal of Computational Physics*, 197:1:215, 2004.
- Moin, P. and Mahesh, K. “Direct numerical simulation: a tool in turbulence research”. *Annual Review of Fluid Mechanics*, 30(1):539–578, 1998.
- Morse, N. and Mahesh, K. “Large-eddy simulation and streamline coordinate analysis of flow over an axisymmetric hull”. *Journal of Fluid Mechanics*, 926:A18, 2021. doi: 10.1017/jfm.2021.714.
- Park, N. and Mahesh, K. “Reduction of the Germano-identity error in the dynamic Smagorinsky model”. *Physics of Fluids* (1994-present), 21(6):065106, 2009.

Posa, A. and Balaras, E. “A numerical investigation of the wake of an axisymmetric body with appendages”. Journal of Fluid Mechanics, 792:470–498, 2016.

Posa, A. and Balaras, E. “A numerical investigation about the effects of reynolds number on the flow around an appended axisymmetric body of revolution”. Journal of Fluid Mechanics, 884, 2020.

Preston, J. H. “The minimum reynolds number for a turbulent boundary layer and the selection of a transition device”. Journal of Fluid Mechanics, 3(4): 373–384, 1958.

Schlatter, P. and Örlü, R. “Turbulent boundary layers at moderate reynolds numbers: inflow length and tripping effects”. Journal of Fluid Mechanics, 710:5–34, 2012. doi: 10.1017/jfm.2012.324.

Swithenbank, S. B., Jessup, S., and Etebari, A. “Measurement of crashback loads on a blade of propeller 4381 in an open and ducted configuration in the 36-inch water tunnel”. Technical Report NSWCCD-50-TR2008/061, Naval Surface Warfare Center Carderock Division Hydromechanics Department Report, 2008.

Verma, A., Jang, H., and Mahesh, K. “The effect of an upstream hull on a propeller in reverse rotation”. Journal of Fluid Mechanics, 704:61–88, 2012.

Vyšohlid, M. and Mahesh, K. “Large eddy simulation of crashback in marine propellers”. In Proceedings of the 26th Symposium on Naval Hydrodynamics, Rome, Italy, 2006.

Yang, C. and Löhner, R. “Prediction of flows over an axisymmetric body with appendages”. In The 8th International Conference on Numerical Ship Hydrodynamics, Busan, Korea, 2003.

DISCUSSION

Michael D. Mattson,

Naval Surface Warfare Center Carderock Division (NSWCCD), Computational Design, Analysis & Development Branch.

I thank the authors for an interesting and wide-ranging paper detailing simulations of submerged bodies with complex geometries, the effect of tripping, the analysis of streamline curvature, and the effect of water tunnel geometry on propeller crashback studies. It is promising for future naval applications that the overset methodology provides greater flexibility and efficiencies, as developing a high-quality grid is a significant effort.

1. The tripping method of wall-normal blowing used a velocity magnitude of 6% of the free-stream, for both tripping on the hull and the appendages. How sensitive is the flow to this parameter?
2. The authors state that the blockage effect in the VPWT for the crashback studies results in a reduced effective advance ratio (J). Have they considered the effect of the incoming boundary layer due the upstream shaft?

AUTHOR'S REPLY

The authors thank you for your comments and questions, which are addressed below.

Question 1: The tripping magnitude was specified as the minimum blowing velocity that caused immediate turbulent transition of the boundary layer. Studies of different tripping velocities showed some local differences in C_p and C_f , but no simulation with the wall-normal blowing trip could reproduce the effect of the resolved experimental trip wire for the appended hull.

Question 2: In general, the boundary layer is considered when studying water tunnel confinement effects. When the boundary layer is very thick, it can have the effect of accelerating the bulk flow experienced by regions of the propeller, increasing the local flow velocity and $\text{mag}(J)$. Meanwhile a velocity deficit and reduction in $\text{mag}(J)$ is possible near the root of the propeller. For these crashback cases, the effects of the boundary layer can be considered negligible. This is because the propeller reverse flow will most likely limit any boundary layer effects to far upstream regions and away from the main flow features like the vortex ring. The blockage ratio is also so high that the effects of solid blockage are much more substantial when compared to all other potential confinement effects of the boundary layer. In addition, there is not enough information on the shaft boundary layer characteristics

from the experiments to make a direct comparison to the simulation results.

DISCUSSION

Hua Shan

Naval Surface Warfare Center, West Bethesda, MD.

The authors should be commended for a very interesting paper demonstrating the LES results of the tripped boundary layer over a SUBOFF and the crash back of an open/ducted P4381 propeller using the overset grid method. In both cases, the LES results were compared with experimental data.

1. The effects of numerical and physical tripping located at $x/D_H = 0.75$ (or $x/L = 0.0872$) on pressure coefficient (C_p) and skin friction coefficient (C_f), pressure distribution, velocity field and profile, and Reynolds stress field and profile were compared and shown in Figs. 7-12. These results show that the difference in the mean and instantaneous flow field quantities is confined to a small region around the tripping location and indicate that the numerical tripping approach might be a good alternative to explicitly resolved trip wire. The height of the trip wire is $0.005D_H$. The Reynolds number based on the height of the trip wire is about 700, which is consistent to the range of critical Reynolds numbers for the trip to be effective. The wall-normal blowing velocity with an amplitude of $0.06U_\infty$ for a numerical tripping is “equivalent” to the physical trip wire with a height of $0.005D_H$, as suggested by the LES results shown in Figs. 7-12. Is there a guidance or procedure to determine the magnitude of blowing velocity corresponding to a specific height of the trip wire? It will also be helpful to investigate this correspondence in the future for an inclined body with small angles.
2. The large fluctuation in side force occurred to a duct propulsor during crash back as shown in Fig. 22 is attributed to the tip-leakage flow and blade local recirculation. It will be helpful to show the time history of the direction or azimuthal angle of the side force, especially during the time when the large fluctuation in side force occurs. A future investigation should consider the wake effect of rudder and stern plane on the magnitude and direction of the side force under a diving/rising or turning condition.

AUTHOR'S REPLY

Thank you for your comments and questions, which are addressed below.

Question 1: Using a simple control volume analysis, it may be possible to specify the blowing velocity to reproduce the same momentum thickness as the experimental trip wire, although this of course ignores local effects of the trip wire on C_p and C_f and requires knowledge of the experimental momentum thickness. Additionally, the numerical blowing method does not necessarily capture the nature of turbulent fluctuations introduced by the trip, which may persist in the boundary layer for an over-tripped configuration. This is of more complex for an inclined body, where quantities such as the local boundary layer thickness and pressure gradient vary at the trip location. The persistence of tripping effects may be significant, and current studies on this topic in the context of LES are ongoing.

Question 2: This behavior is different when looking at different components versus the overall sum. If summed over all components, the behavior is similar to that found in previous publications as the angle remains constant in the specific direction which the vortex ring shedding determines. Individually on the duct, stators, or blades, this angle shows high fluctuations due to local flow characteristics.